Supplemental material for:

Heat current anticorrelation effects leading to thermal conductivity reduction in nanoporous Si

I. Wave-packet simulations

Figure 4 in the main text includes heat maps for some of the wave packet simulations performed in this work. Figures S1–S3 include all the heat maps for the wave packet simulations for the three acoustic modes centered at wave vectors q_o = 0.46, 0.93, 1.45, 1.74, 2.89, 4.05, and 5.21 nm^{-1}. Heat maps are shown for both the 1 nm pore radius, 3.4 nm pore neck (left-hand side plots), and the 2 nm pore radius, 1.4 nm pore neck (right-hand side plots). To tune the wave packets to 5 K, the amplitudes, $\mathcal{A}_o$, of the packets, in ascending order of q_o, are [0.004, 0.002, 0.0016, 0.0012, 0.0010, 0.0006,0.0004, 0.00035] for the longitudinal mode and [0.006, 0.003, 0.0025, 0.0018, 0.0016, 0.0010 ,0.0006, 0.00055] for the transverse mode.

The transmission through the first pore (Fig. 4 (l) in the main text) was computed from the fraction of kinetic energy in the region before the pore ($KE_{emitted}$) at a given time before reflection, and the kinetic energy in the sane region a short time after reflection ($KE_{reflected}$), such that $T = 1 - (KE_{reflected}/KE_{emitted})$. Figure S4 shows the normalized KE during the simulation time for each mode.

Also included is a figure (Fig. 5S) of the vibrational density of states computed for 2ps time intervals during the course of the simulation for the wavepacket simulation in Fig. 4h, for a geometry with 1 nm pores (left-hand plots) and a geometry with 2 nm pores (right-hand plots). In this figure we can see an optical mode show up at ~ 15Hz and the acoustic mode splitting, all happening before the wave reaches the pore. This is due to the anharmonicity in the potential. The aim of this figure is to show that while in Fig. 4h (and others) we observe a split in the velocity of the wavepacket happening at the pores, this is most likely due to the wavepacket being scattered laterally by the curved pore and not due to mode splitting. It can be seen in Fig. 5S, that at ~50 ps, which is when the wave reaches the first pore and a split in velocity is seen in Fig. 4h, and after 50 ps, there is no apparent change in the phonon modes as seen in the VDOS.

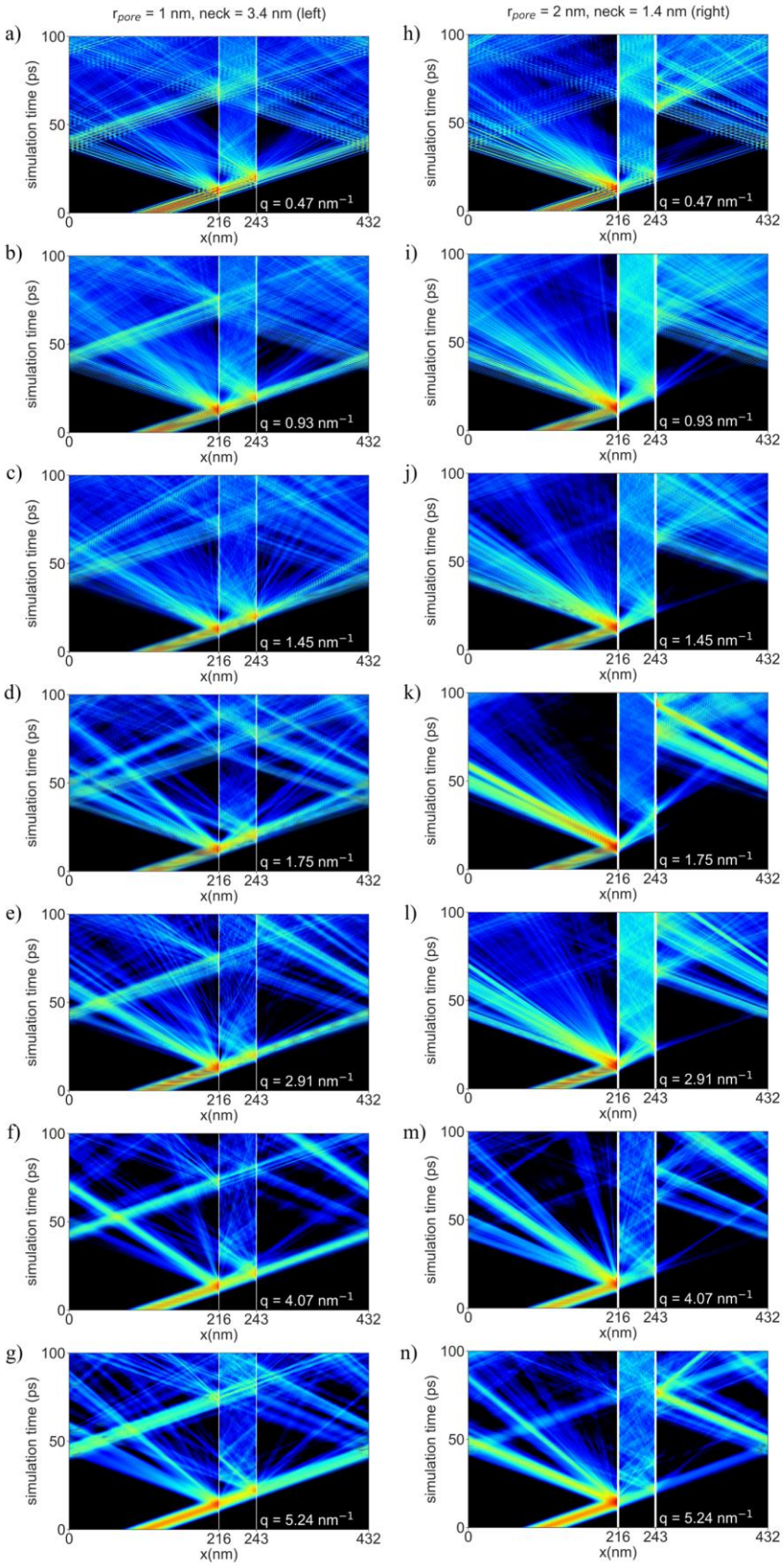

Fig. S1: Heatmap of the evolution of the wave packet kinetic energies during the simulation time along the width of the nanoporous geometries for multiple values of q_o, indicated in each plot, in the longitudinal acoustic (LA) mode. (left) Geometries with a 1nm pore radius and 3.4 nm pore neck, which do not exhibit anticorrelated heat flux in the Green–Kubo calculations. (right) Geometries with a 2nm pore radius and 1.4 nm pore neck, which exhibit the anticorrelation (AC) effect in the Green–Kubo calculations.

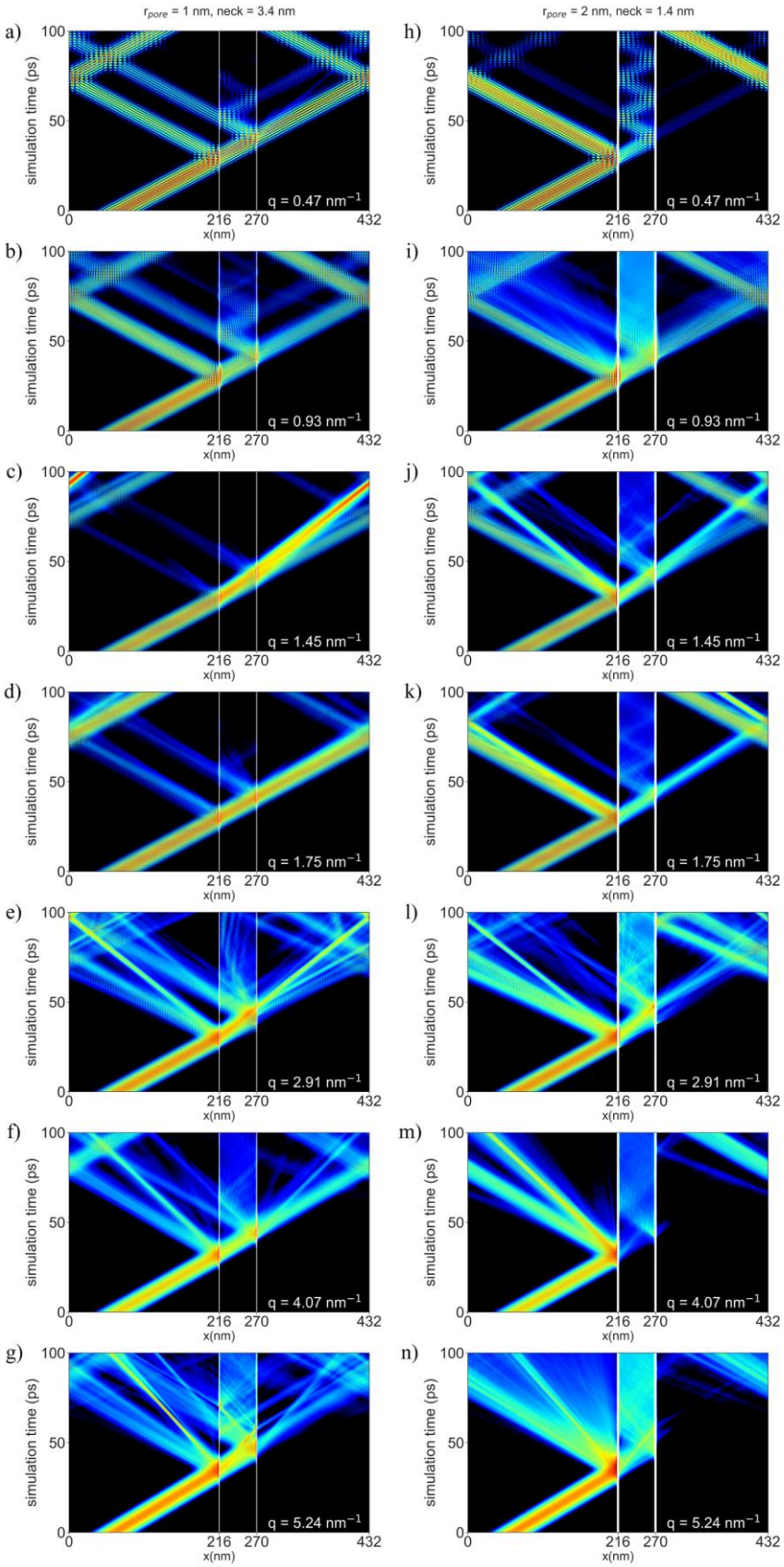

Fig. S2: Same as S1 for the transverse acoustic (TA) mode perpendicular to the cylinder (pore) height orientation.

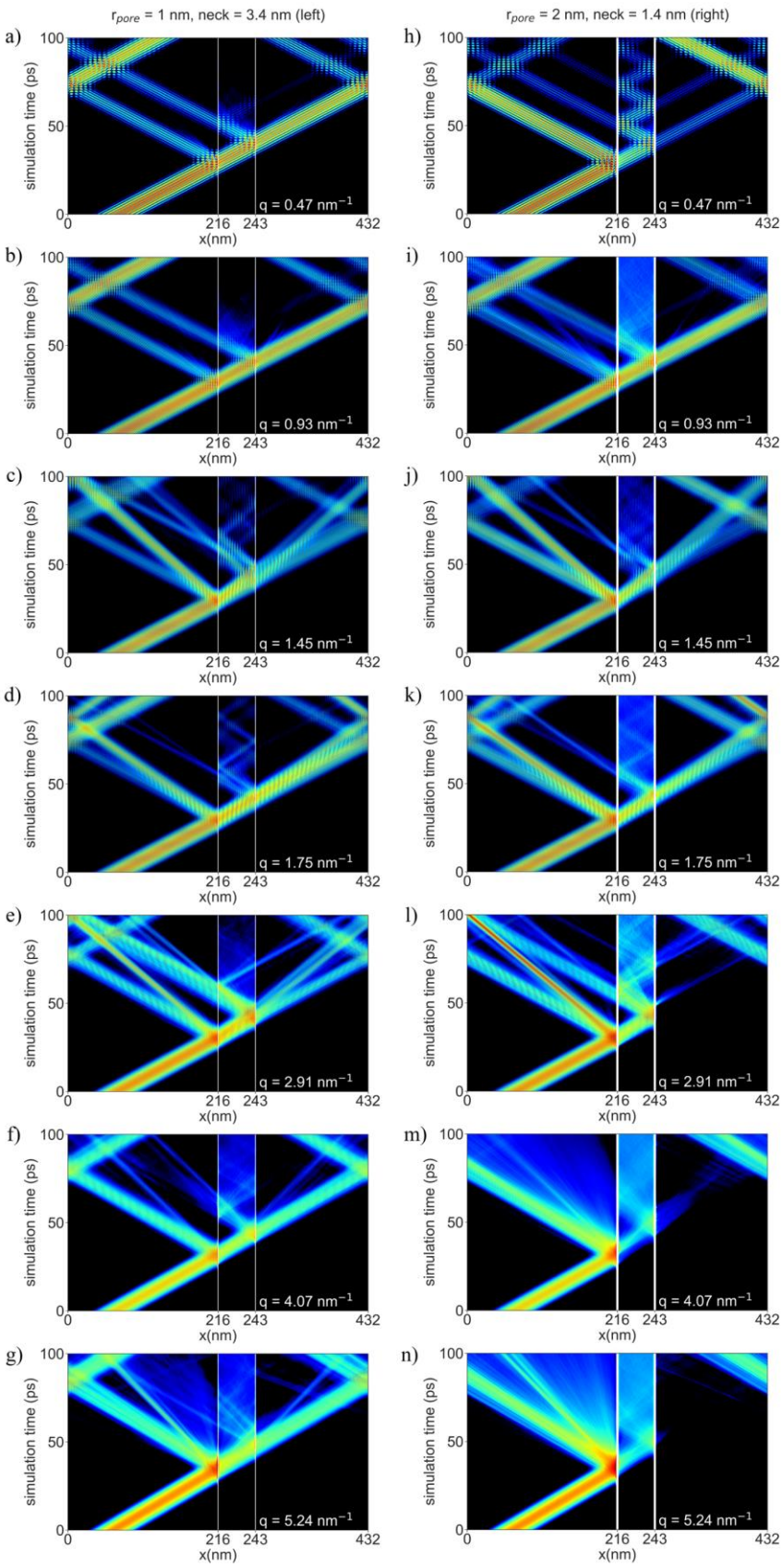

Fig. S3: Same as S1 and S2 for the transverse acoustic (TA) mode parallel to the cylinder (pore) height orientation.

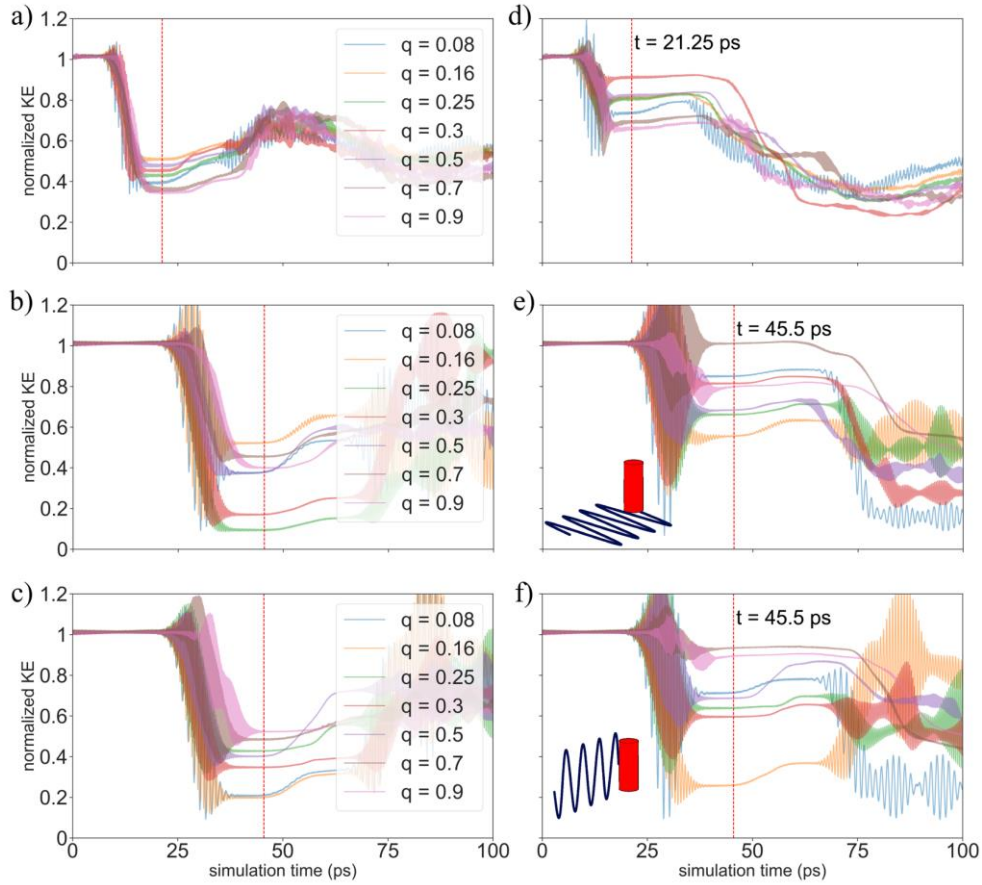

Fig. S4: Normalized kinetic energy for the LA mode in the (a) smaller neck geometry, and (d) the larger pore geometry; the TA mode perpendicular to the height of the pore in the (b) smaller neck geometry, and (e) the larger pore geometry; and the TA mode parallel to the height of the pore in the (c) smaller neck geometry, and (f) the larger pore geometry. The mode polarizations are indicated in the insets.

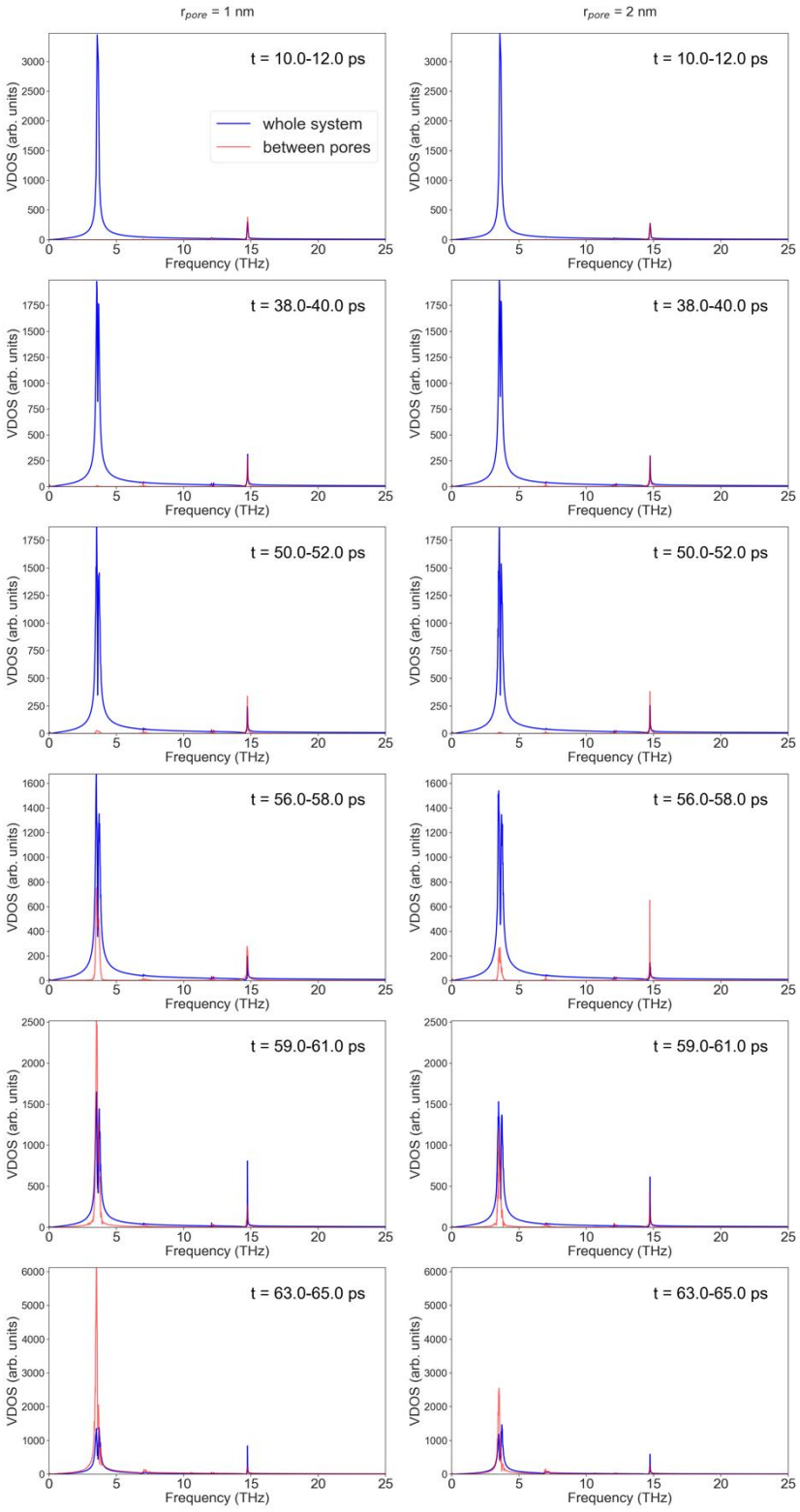

Fig. S5: Vibrational density of states computed for 2ps time intervals during the course of the simulation for the wavepacket simulation in Fig. 4h. The left-hand plots correspond to a geometry with 1 nm pores and the right-hand to a geometry with 2 nm pores. The blue lines show the VDOS for the whole geometry, and the red lines show the VDOS for the region between the pores.

II. Details/derivation of analytical particle model

As indicated in the main text, as a *gedanken* experiment, we consider a simple statistical model of a grey population of heat-carrying acoustic phonons that pop in and out of existence through collisions with a gas of non-propagating optical phonons. The entire system is at thermal equilibrium, and we assume that the acoustic phonons all have the same frequency and group velocity, and their generation and annihilation is random and uncorrelated. Once born, they travel ballistically for a time τ_o (drawn randomly from a Poisson distribution of waiting times with mean lifetime $\bar{\tau}_o$) until they are annihilated by scattering into the optical bath. Each phonon contributes a stepwise heat current, $J_{\mathrm{p}}(t)$ to the total instantaneous heat current given by:

$$J_p(t) = \frac{\omega \hbar v_g}{V} B_p(t - t_p, \tau_p)\widehat{\Omega}_p \,, \tag{2}$$

where $\widehat{\Omega}_p$ is the phonon's direction of travel, and $B_p\big(t - t_p, \tau_p\big)$ is a (discrete) step wise function describing a phonons creation (at time t_p), its annihilation (at interval τ_p later), and any scattering event (as exemplified by the dashed blue line in the top panel of Fig. S1(a)). In Eqn. 2 the terms ω and v_g are the phonons' angular frequency and group velocity respectively. Given the expression (Eqn. 2) for the heat flux of a single phonon, the instantaneous heat current of the entire system is the superposition of $J_{\mathrm{p}}(t)$ from all phonons, so that,

$$J(t) = \frac{\omega \hbar v_g}{V} \sum_{p=1}^{N} B_p\big(t - t_p, \tau_p\big)\widehat{\Omega}_p. \tag{4}$$

The autocorrelation of the heat flux is then the sum of each phonon's cross-correlation with every other phonon (including itself). As the birth and annihilation of a phonon is assumed to be independent of the other phonons the cross-correlation terms will cancel when averaged over sufficient time leaving the autocorrelation function of the total heat current as the weighted average of each phonon's correlation function with itself:

$$\langle J(t)J(t+\tau)\rangle = \frac{1}{3}\frac{\bar{n}_V V}{\bar{\tau}_o}\left(\frac{\omega \hbar v_g}{V}\right)^2 \langle A_p(\tau)\rangle, \tag{5}$$

where $A_p(\tau)$ is the non-normalized and non-averaged autocorrelation of the step function $B_p(t, \tau_o)$ for a phonon with lifetime τ_o, so that:

$$A_p(\tau) = \int_0^\infty B_p(t', \tau_o) B_p(t' + \tau, \tau_o)\, \mathrm{d}t'.$$

For phonons that are not scattered during their lifetime (as depicted by the dashed blue line in Fig. S1(a)) this is the ramp function (dashed green line in Fig. S1(a) with its integral plotted in red) given by:

$$A_p(\tau) = \begin{cases} \tau_o - \tau \; for \; 0 \le \tau \le \tau_o \\ 0 \qquad\qquad \text{otherwise} \end{cases}. \tag{6}$$

In Eq.5 the averaging, $\langle \ldots \rangle$, is performed over all phonon lifetimes with the probability of a phonon having lifetime τ_o given by the Poisson distribution of waiting times $P(\tau_o) = \frac{1}{\bar{\tau}_o} e^{-\frac{\tau_o}{\bar{\tau}_o}}$, where $\bar{\tau}_o$ is the mean phonon lifetime, and thus the integrated HCACF is:

$$\int_0^\infty \langle A_p(\tau') \rangle d\tau' = \int_0^\infty \int_0^{\tau_o} \frac{1}{\bar{\tau}_o} e^{-\frac{\tau_o}{\bar{\tau}_o}} (\tau_o - \tau') d\tau' d\tau_o = {\bar{\tau}_o}^2. \tag{7}$$

Each phonon's contribution to heat transport is proportional to the square of its lifetime, so most of the heat is carried by a minority of long-lived phonons in the tail of the Poisson distribution of lifetimes. As a result, the integral of $\langle A_p(\tau) \rangle$ converges over a correlation time much longer than the average phonon lifetime, consistent with the long correlation times seen in MD.

To explore the effect of specular (perfectly correlated) scattering on the HCACF, we imagine that each acoustic phonon experiences some scattering at a time $\alpha\tau_o$ during its flight that reflects the phonon, reversing its direction, and causing the doubly stepped flux plotted with the solid blue line in Fig. S1(a). The HCACF of these reflected phonons is a three-segment linear piecewise function which can be shown to have the equation:

$$A_{\mathrm{p}}(\tau) = \begin{cases} (\tau_o - 3\tau) & \text{for} \quad \tau \le \tau_o \min(\alpha, 1-\alpha), \\ \tau_o |2\alpha - 1| - \tau & \text{for} \quad \tau_o \min(\alpha, 1-\alpha) < \tau \le \tau_o \max(\alpha, 1-\alpha) \\ (\tau - \tau_o) & \text{for} \quad \tau_o \max(\alpha, 1-\alpha) < \tau \le \tau_o, \\ 0 & \text{otherwise.} \end{cases}. \tag{8}$$

(See solid green line in Fig. S1(a) with its integral plotted in red.) Averaging over a Poisson distribution of lifetimes, and also the distribution of scattering times, gives:

$$\int_0^\infty \langle A_p(\tau') \rangle d\tau' = \int_0^1 \int_0^\infty \int_0^{\tau_o} P_\alpha \frac{1}{\bar{\tau}_o} e^{-\frac{\tau_o}{\bar{\tau}_o}} A_{\mathrm{p}} d\tau' d\tau_o d\alpha = \int_0^1 P_\alpha (1-2\alpha) \, {\bar{\tau}_o}^2 d\alpha, \tag{9}$$

where P_α is the probability distribution that a phonon is reflected at fraction α of the way through its flight. From Eqns. (9) and (7), it follows that the total thermal conductivity reduction due to correlated scattering is:

$$\frac{\kappa_x}{\kappa_o} = \int_0^1 P_\alpha \, (1-2\alpha)^2 d\alpha, \tag{10}$$

where, as mentioned in the main text, P_α is the probability distribution that a phonon is reflected at fraction α of the way through its flight.

III. Thermal conductivity results

It is remarked in the main text that the ratio between the neck and pore diameter is a better metric of the total thermal conductivity than either the neck or pore diameter alone. This has been seen in MC simulations as well, and is clearly shown here in Fig. S6 for the same simulations as in Fig. 2 of the main text. In Fig. S7, corresponding to the same set of simulations as S6, it is shown that negative HCACF values are obtained for geometries with necks upwards of 5 nm.

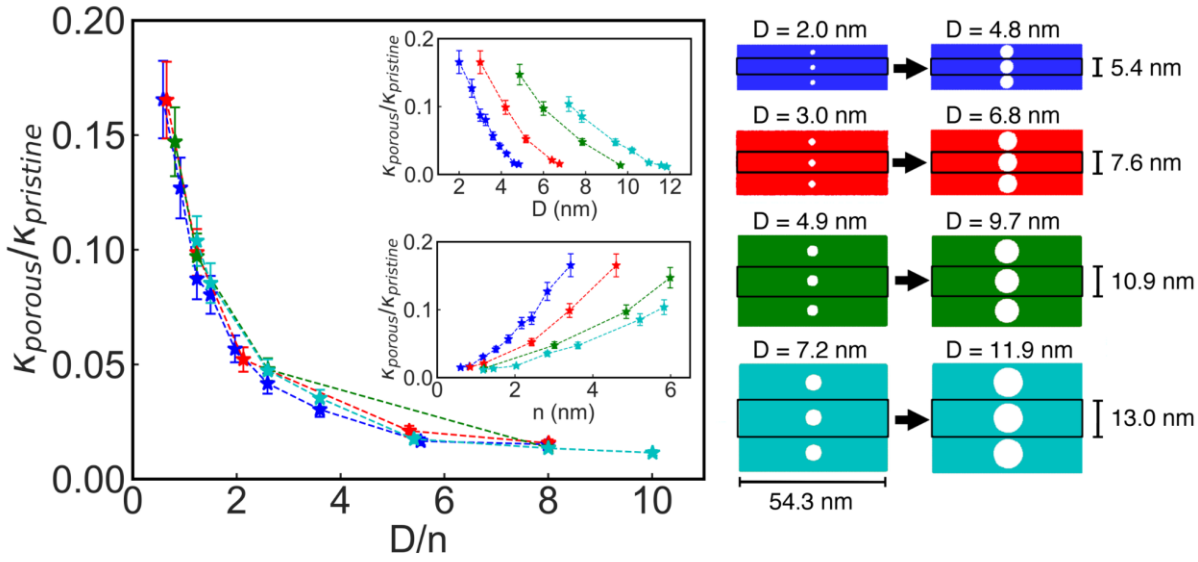

Fig. S6: (left) Fractional thermal conductivity ($\kappa_{porous}/\kappa_{pristine}$) as function of D/n, where D is the pore diameter (i.e., D = 2r), obtained for porous structures using MD simulations. The dashed lines are color-coded according to the size of geometry as shown on the right. (right) Range of geometries simulated. The geometries in blue correspond to a 5.43 nm width and pores with diameters ranging between 2 and 4.8 nm, the red geometries to a 7.6 nm width and pores with diameters ranging between 3.0 and 6.8 nm, the green geometries to a 10.9 nm width and pores with diameters ranging between 4.9 and 9.7 nm, and the cyan geometries to a geometry with a 13 nm width and pores with diameters ranging between 7.2 and 11.9 nm. The simulation length is 54.3 nm for all systems.

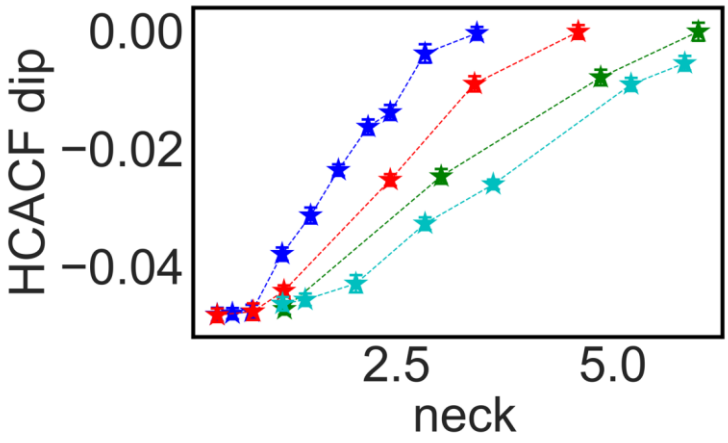

Fig. S7: ‘Height’ of the HCACF dip as a function of the neck size color coded in the same way as Fig. S6.

IV. Other origin considerations for the HCACF AC effect

We find the interpretation that the emergent HCACF dip is a result of specular scattering between the larger pores and smaller necks to be consistent with the results of the wave-packet simulations. Nevertheless, we have considered the possibility that the same (HCACF) behavior could be explained by other mechanisms. For instance, amorphicity near the pores could yield a ‘fluid-like’ atomic oscillation leading to a negative value in the HCACF. Similarly, a softening of the region between the atoms as they get closer together could result in the regions between the pores being able to ‘sway’, which could lead to a similar behavior in the HCACF. Two geometries, with (right) and without (left) a dip in the HCACF, are shown in Fig. S7 at 300 K, indicating that the crystal structure is preserved. This is further supported by the radial distribution analysis in the region between the pores in the course of the simulation. A visual analysis of the stress distribution in the system does also not show any evidence of a softening of the regions between the pores for the same geometries as in S7. Moreover, we would expect that if the negative section of the HCACF was due to oscillations in the regions of the system that are separated by the pores due to softening in the neck region, as in the cartoon picture below, that the negative correlation would have been observed in the *y*- and *z*-directions as well, which is not the case.

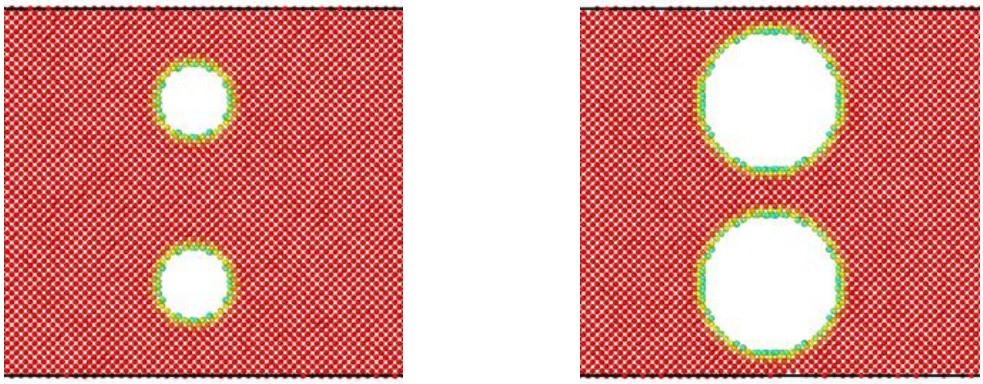

Fig. S7: Coordination analysis around the pore for geometries with (right) and without (left) a dip in the HCACF, at 300 K. Only the region right around the pores has a different coordination than the rest of the geometry. The colors indicate the coordination, with red showing a coordination number of 4, as expected for Si